AIMS Mathematics, 9(6): 16643–16665.
DOI: 10.3934/math.2024807
Received: 18 January 2024
Revised: 25 April 2024
Accepted: 06 May 2024
Published: 14 May 2024

https://www.aimspress.com/journal/Math

Research article

Proximity algorithms for the L^1L^2/TV^α image denoising model

Donghong Zhao*, Ruiying Huang and Li Feng

School of Mathematics and Physics, University of Science and Technology Beijing, Beijing, China

* **Correspondence:** Email: zdh751111@ustb.edu.cn.

Abstract: Inspired by the ROF model and the L^1/TV image denoising model, we propose a combined model to remove Gaussian noise and salt-and-pepper noise simultaneously. This model combines the L^1-data fidelity term, L^2-data fidelity term and a fractional-order total variation regularization term, and is termed the L^1L^2/TV^α model. We have used the proximity algorithm to solve the proposed model. Through this method, the non-differentiable term is solved by using the fixed-point equations of the proximity operator. The numerical experiments show that the proposed model can effectively remove Gaussian noise and salt and pepper noise through implementation of the proximity algorithm. As we varied the fractional order α from 0.8 to 1.9 in increments of 0.1, we observed that different images correspond to different optimal values of α.

Keywords: fractional-order total variation; double fidelity; proximity algorithm; convex minimization problem; image denoising
Mathematics Subject Classification: 49N45, 65K10, 68U10

1. Introduction

Throughout the evolution of digital image processing, a variety of processing technologies have been formed, including the wavelet transform, partial differential equation (PDE), and stochastic model. In image processing, the edge of an image is the most important visual feature. In 1992, Rudin et al. proposed the well-known total variation (TV) model [1], which has been named the ROF model. The ROF model can balance edge preservation and noise removal because it can take advantage of the inherent regularity of the image. The ROF model is as follows:

$$\min_u \int_\Omega \frac{\lambda}{2}||u-u_0||_2^2 + ||u||_{TV}\,\mathrm{d}\Omega, \tag{1}$$

where $\Omega \subset R^n$ is an open bounded set, $n \geq 2$ [2], $u_0(x,y)$ denotes the noisy image and $u(x,y)$ denotes the desired clean image. λ denotes a real positive number and $\|u\|_{TV}$ denotes the TV of $u(x,y)$, which is defined as $\|\nabla u\|_1$. The ROF model has played an important role in image denoising, deblurring and inpainting. However, the solution of the ROF model is a piecewise constant function, so it is easy to generate a blocky effect in the flat region. To reduce the block effect, scholars have proposed a fourth-order PDE [3] and LLT [4], which can effectively remove the noise and reduce the blocky effect. The LLT model is as follows:

$$\min_u \int_\Omega \frac{\lambda}{2}||u-u_0||_2^2 + ||\Delta u||_1\,\mathrm{d}\Omega, \tag{2}$$

where $\Delta u = (\partial_x^2 u, \partial_y^2 u)$ and $\|\Delta u\|_1 = |\partial_x^2 u| + \left|\partial_y^2 u\right|$. The disadvantage of the LLT model is that it produces excessive smoothing in the edge region. To solve this problem, an adaptive fourth-order PDE has been proposed [5]. Both the ROF model and LLT model have the L^2-data fidelity term. The type of noise that corrupts the image typically affects the data fidelity term selection. In general, images are affected by different types of noise. If the image is only affected by a mixture of Gaussian noise and Poisson noise, the noises can be converted into additive Gaussian noise. This is probably why most of the literature is devoted to removing Gaussian noise. The L^2- data fidelity term is suitable for removing Gaussian additive noise, but it is almost invalid for other noises. The L^1-data fidelity term can effectively remove non-additive Gaussian noise, such as Laplacian noise and impulse noise [6,7]. The L^1/TV model is as follows:

$$\min_u \int_\Omega \frac{\lambda}{2}||u-u_0||_1 + ||u||_{TV}\,\mathrm{d}\Omega. \tag{3}$$

The L^1/TV model has some unique features. It does not destroy the geometric structures or morphological invariance of the images under processing [8,9]. Therefore, the L^1/TV denoising image model is widely used in practical applications, such as face recognition [10], shape denoising [11] and image texture decomposition [12]. In fact, images are generally not corrupted by only one type of noise. The mixture of Gaussian and salt-and-pepper noise is considered in this paper. In particular, salt-and-pepper noise is a simple type of impulse noise [13]. An L^1-L^2-data fidelity term was introduced and proved to be suitable for the removal of a mixture of Gaussian and impulse noise in [14]. The L^1L^2/TV model is as follows:

$$\min_u \int_\Omega \lambda||u-u_0||_2^2 + \mu||u-u_0||_1 + ||u||_{TV}\mathrm{d}\Omega, \tag{4}$$

where $\lambda, \mu \geq 0$. The L^1L^2/TV model (4) is a generalization of (1) and (3). For example, if we set $\lambda = 0$ in (4) then we get the L^1/TV model. If we set $\mu = 0$ then we get the L^2/TV model. In particular, the choice of parameters critically affects the quality of image restoration. Small values of λ and μ lead to an oversmoothed reconstruction, which eliminates both noise and detail in the image. In contrast, large values of λ and μ retain noise [15]. An improvement of the L^1L^2/TV model has been proposed in [16], where $\|Wu\|_1$ replaces the TV. In [17], the authors used second-order total generalized variation [18] as a regularization term and incorporated box constraints.

In this paper, the fractional-order TV regularization term is the focus. We propose a combined model with a fractional-order TV regularization term, an L^1-data fidelity term, and an L^2- data fidelity term, which we term the L^1L^2/TV^α model. This model aims to remove the mixture of Gaussian noise and salt-and-pepper noise.

It is difficult to minimize the objective function because the fractional-order TV regularization term is non-differentiable. Numerous efforts have been devoted to addressing this issue. There are some methods to solve the fractional-order TV model, including the use of the primal-dual algorithm [19], fractional-order Euler-Lagrange equations [20], alternating projection algorithm for the fractional-order multi-scale variational model [21,22], and majorization-minimization algorithm [23]. The Split Bregman iterative algorithm [24] and alternating direction method of multipliers [25] can also effectively solve non-differentiable terms. Recently, proximity algorithms [26–30] for solving the ROF model or the L^1/TV denoising image model have attracted widespread attention in digital image processing. The method mainly combines a convex function with a linear transformation to represent the non-differentiable term $\|u\|_{TV}$. The issue of solving the proximity operator of the convex function can be reformulated into solving a fixed-point equation. Consequently, the proximity operator of the convex function can be obtained. The convergence of the fixed-point proximity algorithm has been proven [26]. The L^1/TV model requires solving two fixed point equations due to the non-differentiability of the L^1-data fidelity term [28]. In this paper, the proximity algorithm is used to solve the L^1L^2/TV^α model.

The structure of the paper is as follows. Section 1 introduces the prior works and our motivation. Section 2 proposes the L^1L^2/TV^α model and proves the existence of its solution. The proximity algorithm is applied to solve the model and the convergence of the algorithm is proved. Section 3 presents several numerical experiments and shows the results. Finally, Section 4 concludes the paper.

2. L^1L^2/TV^α denoising model and proximity algorithm

2.1. Proximity operator

This section first introduces two very important concepts of convex functions: the proximity operator and the subdifferential. The relationship between them will also be given.

Initially, we introduce some notations. We denote the m-dimensional Euclidean space by R^m. For $x, y \in R^m$, we define the standard inner product of R^m as $< x, y >:= \sum_{i=1}^m x_i y_i$ and the $p-$ norm of a vector $x \in R^m$as $||x||_p := (\sum_{i=1}^m |x_i|^p)^{\frac{1}{p}}$. The proximity operator was introduced in [31]. We recall its definition as follows.

Definition 2.1. (Proximity operator): Let f be a proper lower-semi-continuous convex function on R^m, where R^m is m-dimensional Euclidean space. The proximity operator of f is defined for any $x \in R^m$ by $prox_f(x) = \arg\min_u \{\frac{1}{2}\|u - x\|_2^2 + f(u): u \in R^m\}$.

Definition 2.2. (Subdifferential): Let f be a proper lower-semi-continuous convex function on R^m, where R^m is m-dimensional Euclidean space. The subdifferential of f is defined for $y \in R^m$ by $\partial f(x) := \{y \in R^m and f(z) \geq f(x) + \langle y, z - x\rangle, \forall z \in R^m\}$.

The following lemma describes the relationship between the proximity operator and the convex function subdifferential.

Lemma 2.1. (Proposition 2.6 in [27]): If f is a convex function on R^m and $x \in R^m$, then

$$y \in \partial f(x) \; if \; and \; only \; if \; x = prox_f(x + y). \tag{5}$$

The proof of this lemma is given in [27]. Based on the Lemma 2.1, we can get that

$$y \in \partial f(x) \; if \; and \; only \; if \; y = (I - prox_f)(x + y). \tag{6}$$

2.2. Model description and analysis

Recently in [13], it has been demonstrated that the L^1L^2/TV model is effective at removing mixtures of Gaussian and impulse noise. In this approach, an image is restored by solving the following equation:

$$\min_p \int_\Omega \lambda||p - p_0||_2^2 + \mu||p - p_0||_1 + ||p||_{TV} \, d\Omega, \tag{7}$$

where $p_0 \in R^{N\times N}$ denotes the noise image, N is a positive integer, $p \in R^{N\times N}$ denotes the denoising image, and λ, μ are the parameters of L^2-data and L^1-data fidelity terms respectively. This model combines two kinds of data fidelity terms, L^1 and L^2, which can combine the advantages of both norms. Therefore, it has a significant effect in the removal of mixtures noise of Gaussian noise and salt-and-pepper noise.

However, we observe that the numerical solution produced by the L^1L^2/TV model yields a substantial block effect. Additionally, this model fails to completely remove salt-and-pepper noise. The fractional-order TV regularization term has been proved to effectively reduce the block effect. This section introduces a minimum optimization denoising model, termed the L^1L^2/TV^α model. The L^1L^2/TV^α model includes three terms: an L^2-data fidelity term for Gaussian noise, an L^1-data fidelity term for salt-and-pepper noise, and a fractional-order TV regularization term for a balance between detail preservation and noise reduction. The model is as follows:

$$\min_p E(p) = \min_p \int_\Omega (\lambda||p - p_0||_2^2 + \mu||p - p_0||_1 + ||p||_{TV^\alpha}) \, \mathrm{d}\Omega, \tag{8}$$

where $p_0 \in R^{N\times N}$ denotes the noise image and $p \in R^{N\times N}$ denotes the denoising image. $\|p\|_{TV^\alpha}$ is the α fractional-order TV of p, and $\|p\|_{TV^\alpha}$ is defined as $\|\nabla^\alpha p\|_1$, where $\nabla^\alpha p = (\partial_x^\alpha p, \partial_y^\alpha p)$ and $\|\nabla^\alpha p\|_1 = |\partial_x^\alpha p| + |\partial_y^\alpha p|$. In particular , note the following:

- When setting $\lambda = 0$, the model (8) simplifies L^1/TV^α.
- When setting $\mu = 0$, the model (8) simplifies L^2/TV^α.

The parameter settings of λ and μ for these specialized models demonstrates the flexibility of the L^1L^2/TV^α model.

To prove the existence of a solution to the L^1L^2/TV^α model, it is critical to prove the boundedness of the potential solution [33].

Lemma 2.2. (Boundedness) Let $p_0 \in L^2(\Omega)$, where $\Omega \subset R^n (n \geq 2)$ is an open bounded set. Given $\inf_\Omega p_0 > 0$, if the model has a solution $\hat{p}$, then $\inf_\Omega p_0 < \hat{p} < \sup_\Omega p_0$.

Proof of Lemma 2.2. Let $\omega = \inf_\Omega p_0$ and $\nu = \sup_\Omega p_0$. When $p > p_0$, functions $|p - p_0|$ and

$(p-p_0)^2$ increase monotonically. Then,

$$\int_\Omega ||inf(p,v)-p_0||_1 \mathrm{d}\Omega \le \int_\Omega ||p-p_0||_1 \mathrm{d}\Omega, \tag{9}$$

$$\int_\Omega \|inf(p,v)-p_0\|_2^2 \mathrm{d}\Omega \le \int_\Omega \|p-p_0\|_2^2 \mathrm{d}\Omega, \tag{10}$$

where $inf(p,v)$ is the lower bound of p and v. That is, $inf(p,v)$ is the minimum value of p and v.

Moreover, based on Lemma 2 in the literature [34], there exists $TV^\alpha(inf(p,v)) \le TV^\alpha(p)$. Thus, we have

$$E(inf(p,v)) \le E(p), \tag{11}$$

and the equation holds if and only if $p \le v$.

Since $\hat{p}$ is the minimum solution of optimization problem (8), the equation holds when $p=\hat{p}$ and hence $\hat{p} \le v$. Similarly, $E(p) \le E(sup(p,\omega))$; then, $\hat{p} \ge \omega$ can be obtained. In summary, $\inf\limits_{\Omega} f < \hat{p} < \sup\limits_{\Omega} f$.

In what follows, we will give the existence of a solution for the optimization problem (8).

Lemma 2.3. (Existence): Let $p_0 \in L^2(\Omega)$, where $\Omega \subset R^n (n \ge 2)$ is an open bounded set. Given $\inf\limits_{\Omega} p_0 > 0$, the optimization problem (8) has at least one solution in the solution space $BV^\alpha(\Omega)$.

Proof of Lemma 2.3. The space of bounded variational functions $BV^\alpha(\Omega)$ can be defined as follows: $BV^\alpha(\Omega)=\{f: f \in L^1(\Omega)\}$, forming Banach spaces under the BV^α norm $\|f\|_{BV^\alpha} = \|f\|_{L^1} + TV^\alpha(f)$.

Define $\omega = \inf\limits_{\Omega} p_0$ and $v = \sup\limits_{\Omega} p_0$. Because $p = v \in BV^\alpha(\Omega)$, the solution space is not empty [35]. Consider that the optimization problem (8) has a minimization sequence $\{p_n\} \in BV^\alpha(\Omega)$ with $\omega \le p_n \le v$.

Because $BV^\alpha(\Omega)$ is a Banach space and Ω is bounded, it follows that

$$\|p_n\|_{L^1} = \int_\Omega |p_n| \mathrm{d}\Omega \le +\infty. \tag{12}$$

Moreover, because $\{p_n\}$ is a minimization sequence, there exists a constant $C>0$ such that $E(p_n) \le C$. Because $\int_\Omega ||p-p_0||_2^2 + ||p-p_0||_1 d\Omega$ is nonnegative, there is a constant $C'>0$ and

$$TV^\alpha(p_n) \le C'. \tag{13}$$

Equations (12) and (13) yield that $\{p_n\}$ is consistently bounded. Due to the compactness of $BV^\alpha(\Omega)$, there exists a subsequence $\{p_{n_j}\}$ of $\{p_n\}$ and a function $p \epsilon BV^\alpha(\Omega)$ such that

$$\{p_{n_j}\} \to p, in\ L^1(\Omega).$$

Using the Lebesgue control convergence theorem, we obtain

$$\int_{\Omega} ||p - p_0||_1 d\Omega = \lim_{j\to\infty} \int_{\Omega} ||p_{n_j} - p_0||_1 d\Omega, \tag{14}$$

$$\int_{\Omega} ||p - p_0||_2^2 d\Omega = \lim_{j\to\infty} \int_{\Omega} ||p_{n_j} - p_0||_2^2 d\Omega. \tag{15}$$

According to the lower semi-continuity of the function, the following inequality holds:

$$E(p) \leq \lim_{n\to\infty} inf\ E(p_n). \tag{16}$$

Since $\{p_n\}$ is a minimization sequence, p is the smallest solution to the optimization problem (8).

2.3. Numerical algorithm and convergence analysis

Consider an image represented by a grid of $N \times N$ pixels. The discretization of the data term is given by

$$\int_{\Omega} ||p - p_0||_2^2 \, \mathrm{d}\Omega \approx \sum_{i,j} \left(p_{i,j} - p_{0i,j}\right)^2, \ \int_{\Omega} \|p - p_0\|_1 \, \mathrm{d}\Omega \approx \sum_{i,j} \left|p_{i,j} - p_{0i,j}\right|,$$

where (i, j) denotes the coordinates at the points. For the fractional-order TV term, we obtain the following discretization:

$$\int_{\Omega} \|\nabla^{\alpha} p\|_1 \, \mathrm{d}\Omega \approx \sum_{i,j} \left|\nabla_x^{\alpha} p_{i,j}\right| + \left|\nabla_y^{\alpha} p_{i,j}\right|,$$

$$\nabla_x^{\alpha} p_{i,j} = \sum_{k=0}^{K-1} (-1)^k C_k^{\alpha} p_{i-k,j}, \ \nabla_y^{\alpha} p_{i,j} = \sum_{k=0}^{K-1} (-1)^k C_k^{\alpha} p_{i,j-k},$$

where $C_k^{(\alpha)} = (-1)^{\alpha} \frac{\Gamma(\alpha+1)}{\Gamma(k+1)\Gamma(\alpha-k+1)}$ and $\Gamma(x)$ is the gamma function.

Considering that the proximity algorithm is suitable for vectors, we respectively transform the image matrices p and p_0 into vectors u and u_0 by using the formulas $p_{i,j} = u_{(j-1)n+i}$ and $p_{0i,j} = u_{0_{(j-1)n+i}}$, $i, j = 1,2, \ldots, N$. We describe the minimization problem (8) as follows:

$$\arg\min_{u} \ \{\lambda ||u - u_0||_2^2 + \mu ||u - u_0||_1 + ||\nabla^{\alpha} u||_1\}, \tag{17}$$

where $u \in R^m$ and $u_0 \in R^m, m = N^2$.

The proximity operator of $\|\nabla^{\alpha} u\|_1$ is not easy to compute. To overcome this difficulty, we treat $\|\nabla^{\alpha} u\|_1$ as the composition of a convex function with a fractional-order difference operator by using the formula $\|\nabla^{\alpha} u\|_1 = (\phi \circ B^{\alpha})(u)$. In the formula, $\phi: R^{2m} \to R$ is defined as the norm $\|\cdot\|_1, B^{\alpha}$ is a $2m \times m$ matrix, and $\nabla^{\alpha} u$ can be represented as $B^{\alpha} u$. The (i, j) component of $\nabla^{\alpha} u$ can thus be represented as a multiplication of the vector $u \in R^m$ by a matrix $B_n^{\alpha} \in R^{2\times m}$ for $n = 1, 2, \ldots, m$:

$$B_n^\alpha u = \begin{cases} (\sum_{k=0}^{i-1} C_k^{(a)} u_{n-k}, \sum_{k=0}^{j-1} C_k^{(a)} u_{n-Nk})^T & i > 1, j > 1 \\ (u_m, \sum_{k=0}^{j-1} C_k^{(a)} u_{n-Nk})^T & i = 1, j > 1 \\ (\sum_{k=0}^{i-1} C_k^{(a)} u_{n-k}, u_n)^T & i > 1, j = 1 \\ (u_n, u_n)^T & i = 1, j = 1 \end{cases}, \tag{18}$$

where the matrix $B_n^\alpha = [B_1^\alpha, B_2^\alpha, \dots, B_N^\alpha]^T \in R^{2\times 2m}$ [29]. Therefore, we describe the minimization problem as follows:

$$\arg\min_u \{\lambda \big||u - u_0||_2^2 + \mu \big||u - u_0||_1 + (\phi \circ B^\alpha)(u)\}. \tag{19}$$

Consider φ to be a convex function on R^m at $u \in R^m$, as follows:

$$\varphi(u) = \lambda \big||u - u_0||_2^2 + \mu \big||u - u_0||_1. \tag{20}$$

Therefore, we can describe the above minimization problem as follows:

$$\arg\min_u \{\varphi(u) + (\phi \circ B^\alpha)(u)\}. \tag{21}$$

Proposition 2.1. Let ϕ be a proper convex function on R^m; B^α is a $2m \times m$ matrix. If $u \in R^m$ is a solution of model (21), then for any positive numbers $\beta_1,\ \beta_2 > 0$, there exists a vector $b \in R^{2m}$ such that

$$u = prox_{\frac{1}{\alpha}\varphi}(u - \frac{\beta_2}{\beta_1}(B^\alpha)^T b), \tag{22}$$

$$b = \left(I - prox_{\frac{1}{\beta_2}\phi}\right)(B^\alpha u + b). \tag{23}$$

On the contrary, if $b \in R^{2m}$ and $u \in R^m$ satisfies (22) and (23) for some positive $\beta_1,\ \beta_2 > 0$, then u is a solution of (21).

Proof. If $u \in R^m$ is a solution of (21), then, by Fermat's theorem on convex analysis, it follows that

$$0 \in \partial(\varphi(u) + (\phi \circ B^\alpha)(u)).$$

By the chain rule

$$\partial\big((\phi \circ B^\alpha)(u)\big) = (B^\alpha)^T \partial\phi(B^\alpha u),$$

then

$$0 \in \partial\varphi(u) + (B^\alpha)^T\, \partial\phi(B^\alpha u). \tag{24}$$

For any $\beta_1,\ \beta_2 > 0$, we choose two vectors $a \in \frac{1}{\beta_1}\partial\varphi(u)$ and $b \in \frac{1}{\beta_2}\partial\phi(B^a u)$ such that

$$0 = \beta_1 a + \beta_2 (B^\alpha)^T b. \tag{25}$$

By (5) and $a \in \frac{1}{\beta_1}\partial\varphi(u)$, we have that

$$u = prox_{\frac{1}{\beta_1}\varphi}(u + a). \tag{26}$$

Using (25), we conclude that $a = -\frac{\beta_2}{\beta_1}(B^\alpha)^T b$; by substituting a into (26), we obtain (22). By applying the definition of the proximity operator and $b \in \frac{1}{\beta_2}\partial\phi(B^\alpha u)$, we obtain (23). Conversely, if there exist $\beta_1, \beta_2 > 0$, $b \in R^{2m}$, and $u \in R^m$ satisfying (22) and (23), then by Lemma 2.1, we obtain that $b \in \frac{1}{\beta_2}\partial\phi(B^\alpha u)$ and $-\frac{\beta_2}{\beta_1}(B^\alpha)^T b \in \frac{1}{\alpha}\partial\varphi(u)$. We can yield that

$$0 = \beta_1\left(-\frac{\beta_2}{\beta_1}(B^\alpha)^T b\right) + \beta(B^\alpha)^T b \in \partial\varphi(u) + (B^\alpha)^T \partial\varphi(B^\alpha u).$$

This implies that $u \in R^m$ is a solution of (21).

According to Proposition 2.1, we can conclude the following corollary.

Corollary 2.1. Suppose that $u_0 \in R^m$ is given, λ, μ are two positive numbers, B^α is a $2m \times m$ matrix, φ is the function defined by (12), and ϕ is a differentiable convex function on R^{2m}. If $u \in R^m$ is a solution of (21), then for any $\beta_1 > 0$,

$$u = prox_{\frac{1}{\beta_1}\varphi}(u - \frac{1}{\beta_1}(B^\alpha)^T \partial\phi(B^\alpha u)). \tag{27}$$

Conversely, if for some $\beta_1 > 0$ there exists $u \in R^m$ satisfying (27), then $u \in R^m$ is a solution to (21).

Proof. By Proposition 2.1, a solution $u \in R^m$ of (21) satisfies (22) and (23). If the function ϕ is differentiable, then $\partial\phi(u) = \{\nabla\phi(u)\}$, where $\partial\phi(u)$ is the gradient of ϕ at u. Therefore, (6) and (23) imply that $b = \frac{1}{\beta_2}\partial\phi(B^\alpha u)$. Hence, (22) yields the fixed-point equation (27).

The fixed-point equation (27) can be viewed as an instance of the split forward-backward formula [31]. Suppose that $\partial\phi$ is Lipschitz continuous with a Lipschitz constant L, that is

$$\left|\left|\partial\phi(p) - \partial\phi(q)\right|\right|_2 \leq L\left|\left|p - q\right|\right|_2, \forall p, q \in R^m, \tag{28}$$

and that β_1 is chosen to satisfy

$$\frac{1}{\beta_1} < \frac{2}{L||B^\alpha||_2^2}. \tag{29}$$

It was proved in [33], that for any initial point $u^0 \in R^m$, the Picard iteration

$$u^{k+1} = prox_{\frac{1}{\beta_1}\varphi}(u^k - \frac{1}{\beta_1}(B^\alpha)^T \partial\phi(B^\alpha u^k)), \tag{30}$$

converges to a fixed point of (27), which is a minimum of (21).

Let $Hu := u - \frac{1}{\beta_1}(B^\alpha)^T \partial\phi(B^\alpha u^k)$ and $Qu := (prox_{\frac{1}{\beta_1}\varphi} \circ H)u$. To prove that (30) is convergent, we only need to prove that H and Q are non-expansive averaged operators. We recall the definitions of non-expansive operators [31].

Definition 2.3. (Non-expansive operator): An operator T on R^m is non-expansive if it satisfies the following condition $\forall x, y \in R^m$: $\|Tx - Ty\|_2 \leq \|x - y\|_2$.

Both $prox_f(x)$ and $(I - prox_f)(x)$ are operators; see [31].

Definition 2.4. (Firmly non-expansive operator): An operator T on R^m is firmly non-expansive if it satisfies the following condition $\forall x, y \in R^m$: $\|Tx - Ty\|^2 \leq < x - y, Tx - Ty >$.

Definition 2.5. (Non-expansive averaged operators): A non-expansive operator Q on R^m is a non-expansive averaged operator if there exists $k \in (0,1)$ and it satisfies the following condition $\forall x, y \in R^m$: $Q = kI + (1-k)P$, where P is a non-expansive operator. If $k = \frac{1}{2}$, then Q is a firmly non-expansive operator.

Both $prox_f(x)$ and $(I - prox_f)(x)$ are firmly non-expansive operators; see [32].

Proposition 2.2. If ϕ is a convex function and B^α is a $2m \times m$ matrix, then H is firmly non-expansive.

Proof. First, by the definition of the operator H, $\forall x, y \in R^m$, we have

$$Hx - Hy = x - y - \frac{1}{\beta_1}(B^\alpha)^T(\partial\phi(B^\alpha x) - \partial\phi(B^\alpha y)), \tag{31}$$

$$(I - H)x - (I - H)y = \frac{1}{\beta_1}(B^\alpha)^T(\partial\phi(B^\alpha x) - \partial\phi(B^\alpha y)). \tag{32}$$

We have

$$\| Hx - Hy \|^2 = \| x - y \|^2 - \frac{2}{\beta_1}\langle (B^\alpha)^T\big(\partial\phi(B^\alpha x) - \partial\phi(B^\alpha y)\big), x - y\rangle + \frac{1}{\beta_1{}^2}\big\|(B^\alpha)^T\big(\partial\phi(B^\alpha x) - \partial\phi(B^\alpha y)\big)\big\|^2, \tag{33}$$

$$\|(I - H)x - (I - H)y\|^2 = \frac{1}{\beta_1{}^2}\| (B^\alpha)^T(\partial\phi(B^\alpha x) - \partial\phi(B^\alpha y)) \|^2. \tag{34}$$

According to the sub-gradient inequalities of convex functions, we have

$$\langle \partial\phi(B^\alpha x) - \partial\phi(B^\alpha y), B^\alpha x - B^\alpha y\rangle \geq 0. \tag{35}$$

Substituting (35) into (33), we have

$$\| Hx - Hy \|^2 \leq \| x - y \|^2 + \frac{1}{\beta_1{}^2}\| (B^\alpha)^T(\partial\phi(B^\alpha x) - \partial\phi(B^\alpha y)) \|^2. \tag{36}$$

Combining (36) with (34), we have

$$\| Hx - Hy \|^2 \leq \| x - y \|^2 + \| (I - H)x - (I - H)y \|^2. \tag{37}$$

We have

$$\|Hx - Hy\|^2 \leq < x - y, Hx - Hy >.$$

This completes the proof.

If $H: R^m \to R^m$ is firmly non-expansive, then H is a non-expansive $\frac{1}{2}$-averaged operator (see Lemma 3.8 in [26]). Thus Q is a non-expansive averaged operator (see Lemma 3.7 in [26]).

We prove the convergence of (30). To simplify (30) and find an iterative format that is equivalent to (30), we make the following substitution

$$u^k - \frac{1}{\beta_1}(B^\alpha)^T \partial\phi(B^\alpha u^k) = v. \tag{38}$$

Let $v \in R^m$ be a given vector and $x \in R^m$; we denote the proximity operator of $\frac{1}{\beta_1}\varphi$ for the given $v \in R^m$ as follows

$$prox_{\frac{1}{\beta_1}\varphi}(v) = \arg\min_x \{\frac{1}{2}||x - v||_2^2 + \frac{\lambda}{\beta_1}||x - u_0||_2^2 + \frac{\mu}{\beta_1}||x - u_0||_1\}. \tag{39}$$

We have

$$prox_{\frac{1}{\beta_1}\varphi}(v) = u_0 + \arg\min_x \{\frac{1}{2}||x - v + u_0||_2^2 + \frac{\lambda}{\beta_1}||x||_2^2 + \frac{\mu}{\beta_1}||x||_1\}. \tag{40}$$

Let g and f be two functions on R^m; then, we have

$$g(x) = \frac{1}{2}||x - v + u_0||_2^2 + \frac{\lambda}{\beta_1}||x||_2^2, \tag{41}$$

$$f(x) = \frac{\mu}{\beta_1}||x||_1. \tag{42}$$

Because the function g is differentiable, it can be expanded by applying the Taylor formula to $(v - u_0) \in R^m$:

$$g(x) = g(v - u_0) + < \nabla g(v - u_0), x - v + u_0 > + \frac{1}{2r}||x - v + u_0||_2^2, \tag{43}$$

where r denotes a constant greater than 1.

We can use (43) to find the following minimum value problem:

$$\begin{aligned} &\arg\min_x \{g(x) + f(x)\} \\ &= \arg\min_x \left\{g(v - u_0) + < \nabla g(v - u_0), x - v + u_0 > + \frac{1}{2r}\left||x - v + u_0||_2^2 + f(x)\right.\right\} \\ &= \arg\min_x \left\{\frac{1}{2r}\left||x - v + u_0 + r\nabla g(v - u_0)||_2^2 + f(x)\right.\right\} \\ &= prox_{rf}\big(v - u_0 - r\nabla g(v - u_0)\big). \end{aligned} \tag{44}$$

By (41), we can get

$$\nabla g(x) = (x - v + u_0) + \frac{\lambda}{2\beta_1}x = \left(1 + \frac{2\lambda}{\beta_1}\right)x - v + u_0. \tag{45}$$

Using (45), we obtain

$$\nabla g(v-u_0)=\frac{2\lambda}{\beta_1}(v-u_0). \tag{46}$$

Therefore, substituting (42), (44) and (46) into (40), we conclude that

$$prox_{\frac{1}{\beta_1}\varphi}(v)=u_0+prox_{\frac{r\mu}{\beta_1}||\cdot||_1}\left(\frac{\beta_1-2\lambda r}{\beta_1}(v-u_0)\right). \tag{47}$$

We can combine (38) and $u^{k+1}=prox_{\frac{1}{\beta_1}\varphi}(v)$ with (47) to obtain

$$u_{k+1}=u_0+prox_{\frac{r\mu}{\beta_1}||\cdot||_1}(\frac{\beta_1-2\lambda r}{\beta_1}(u_k-\frac{1}{\alpha}(B^\alpha)^T\,\partial\phi(B^\alpha p^k)-u_0)). \tag{48}$$

Substituting $b^k=\frac{1}{\beta_2}\partial\phi(B^\alpha u^k)$ into (48) shows that (49) and (50) are equivalent iterations of (30).

$$u_{k+1}\quad=u_0+prox_{\frac{r\mu}{\beta_1}||\cdot||_1}(\frac{\beta_1-2\lambda r}{\beta_1}(u_k-\frac{\beta_2}{\beta_1}(B^\alpha)^T b^k-u_0)), \tag{49}$$

$$b^{k+1}\quad=\left(I-prox_{\frac{1}{\beta_2}\phi}\right)(B^\alpha u^{k+1}+b^k). \tag{50}$$

Hence, according to the iterative equations (48) and (49), We can propose the following algorithm.

Algorithm

1. Noisy image $u_0\in R^m$; choose $\lambda\geq 0,\ \mu\geq 0,\ \beta_1>0,\ \beta_2>0$;
2. Initialization: $u^0=p_0,\ b^0=0$;
3. For $k\in N$, update u and b as follows:

$$u^{k+1}\leftarrow u_0+prox_{\frac{r\mu}{\beta_1}||\cdot||_1}(\frac{\beta_1-2\lambda r}{\beta_1}(u^k-\frac{1}{\beta_1}(B^\alpha)^T b^k-u_0))$$

$$b^{k+1}\leftarrow(I-prox_{\frac{1}{\beta_2}\phi})(B^\alpha u^{k+1}+b)$$

4. Stop if the preset stop criteria are met; otherwise, return to 2 to continue iteration.

3. Numerical results

This section describes several image denoising experiments that were conducted to demonstrate the behavior of the proposed algorithm. The peak signal to noise ratio (PSNR) is currently the most widely used tool for objectively evaluating image quality, and it is consistent with human subjective perception. A larger value of PSNR indicates better quality of the recovered image. It is defined as follows:

$$\text{PSNR}=10log_{10}\frac{255^2n^2}{||u^*-u||_2^2}(dB), \tag{51}$$

where u^* is the original image and u is the denoised image. All experiments' iterations were ceased

when the following criterion was satisfied:

$$\frac{\left||u^k - u^{k+1}|\right|}{\left||u^{k+1}|\right|} \leq 0.001. \tag{52}$$

In this study, images of size 256×256 pixels were used to conduct numerical experiments with $r = \frac{\beta_1}{\beta_1 + 2\lambda}$. We used the L^1L^2/TV^α model to remove Gaussian noise, salt-and-pepper noise, and mixed noise. Original images of the experiment are shown in Figure 1. In particular, the different noise regimes yielded different results, as shown in Figure 2. Salt-and-pepper noise involves setting a value of a pixel to the minimal or maximal value of the image intensity range. Gaussian noise may extend this intensity range. We considered adding salt-and-pepper noise to the original image after Gaussian noise.

Figure 1. Original images.

Figure 2. (a) image is affected by salt-and-pepper noise after Gaussian noise; (b) image affected by Gaussian noise after salt-and-pepper noise.

This study included a total of four groups of experiments. The first experiment was to restore

images affected with $\sigma = 20$, which is the level of Gaussian noise. The second experiment was to restore images affected with $s = 0.03$, which is the level of salt-and-pepper noise. The third experiment was to restore images affected by the mixed noise. The fourth experiment was to explore the convergence of our proposed fractional-order TV denoising algorithm.

We began by investigating the effects of different parameters on the experimental results. Inspired by [27], we consistently chose $\alpha = 6, \beta = 128$. We determined the most suitable values λ and μ through trial and error. When Gaussian noise with $\sigma = 20$ was added to the image 'Lena', we found that $\lambda = 0.07, \mu = 0$ performed better. When salt-and-pepper noise with $s = 0.03$ was added to the image 'Square', we found that $\lambda = 0, \mu = 3$ performed better. We verified that these selected parameters were effective for other images with the same noise levels. Additionally, we increased α from 0.8 to 1.9 in increments of 0.1.

In the first experiment, the Gaussian noise was added to the 'Lena' image at different levels. We chose $\lambda = 0.07, \mu = 0$ to deal with noisy images. Table 1 shows the values of PSNR, while Figure 3 shows the experimental results. In addition, Gaussian noise was added to the other images at $\sigma = 20$. Table 2 shows the values of PSNR. The first experimental results demonstrated that α has an impact on the denoising results. The best denoising result often did not appear when $\alpha = 1$. Therefore, the fractional-order TV model can be applied to improve the denoising performance of the TV model.

(a) Lena with noisy $\sigma = 20$ (b) Denoised image when α=1 (c) Denoised image when α=1.5 (d) Denoised image when $\alpha = 1.8$

Figure 3. Comparison of visual results with different values of α for the noisy image at $\sigma = 20$.

Table 1. PSNR values for the different Gaussian noise levels.

α	$\sigma = 15$	$\sigma = 20$	$\sigma = 25$	$\sigma = 30$
0.8	29.7892	27.4593	25.0759	23.0262
0.9	30.2569	27.8891	25.4172	23.3055
1	30.5238	28.2065	25.7044	23.5671
1.1	**30.5492**	28.3853	25.9207	23.7875
1.2	30.5086	28.5046	25.1172	24.0012
1.3	30.4731	28.6112	26.3034	24.2273
1.4	30.4378	28.7046	26.4887	24.4474
1.5	30.3991	28.7886	26.6701	24.6726
1.6	30.3599	28.8649	26.8453	24.8976
1.7	30.3170	28.9319	27.0052	25.1174
1.8	30.2558	28.9798	27.1521	25.3290
1.9	30.1917	**29.0035**	**27.2755**	**25.5298**

Table 2. PSNR values for the noisy images with $\sigma = 20$.

α	Man	Pepper	Square
0.8	27.5666	27.3701	29.7428
0.9	27.9925	27.8178	30.4608
1	28.2736	28.1412	31.8894
1.1	28.3151	28.1936	31.1472
1.2	**28.2914**	28.3959	31.3280
1.3	28.2809	28.4796	31.4950
1.4	28.2808	28.5583	31.6557
1.5	28.2824	28.6456	31.8110
1.6	28.2666	28.7134	31.9377
1.7	28.2452	28.7684	32.0184
1.8	28.2056	28.8044	**32.0599**
1.9	28.1466	**29.8223**	32.0439

In the second experiment, we chose $\lambda = 0$, $\mu = 4.8$ to deal with the 'Square' image corrupted by the salt-and-pepper noise at noise levels of 0.01, 0.02, 0.03, 0.05. Table 3 shows the values of PSNR, while Figure 4 shows the experimental results. In addition, salt-and-pepper noise was applied to the other images at $s = 0.03$. Table 4 shows the values of PSNR. The experimental results indicate that when α is larger, the effect is better.

Table 3. PSNR values for the different salt-and-pepper noise levels.

α	$s = 0.01$	$s = 0.02$	$s = 0.03$	$s = 0.05$
0.8	26.6361	23.5071	21.5444	19.3476
0.9	26.8099	23.6805	21.7061	19.5088
1	26.9692	23.8357	21.8529	19.6589
1.1	27.184	24.0518	22.0587	19.8782
1.2	27.3262	24.1908	22.1921	20.0358
1.3	28.6720	25.4874	23.4443	21.2008
1.4	30.3872	27.1640	25.0587	22.7285
1.5	32.3797	29.0880	26.8780	24.4160
1.6	34.7346	31.2814	26.8750	26.2035
1.7	37.4620	33.7378	30.9774	27.7989
1.8	40.4214	36.6253	33.2592	30.0331
1.9	**42.8820**	**39.2325**	**35.0649**	**31.0890**

Table 4. PSNR values for the different salt-and-pepper noise levels.

α	Lena	Man	Pepper
0.8	22.4379	22.3227	22.5437
0.9	22.7182	22.5793	22.8359
1	22.9806	22.8058	23.1135
1.1	23.2306	23.0675	23.3906
1.2	23.4360	23.2628	23.6167
1.3	24.7680	24.4272	24.8107
1.4	26.8144	26.1801	26.6391
1.5	29.1850	28.1721	28.6084
1.6	31.5879	30.1103	30.4547
1.7	33.4039	31.3361	31.7732
1.8	34.7360	31.8994	**32.7549**
1.9	**35.4855**	**32.2108**	32.4564

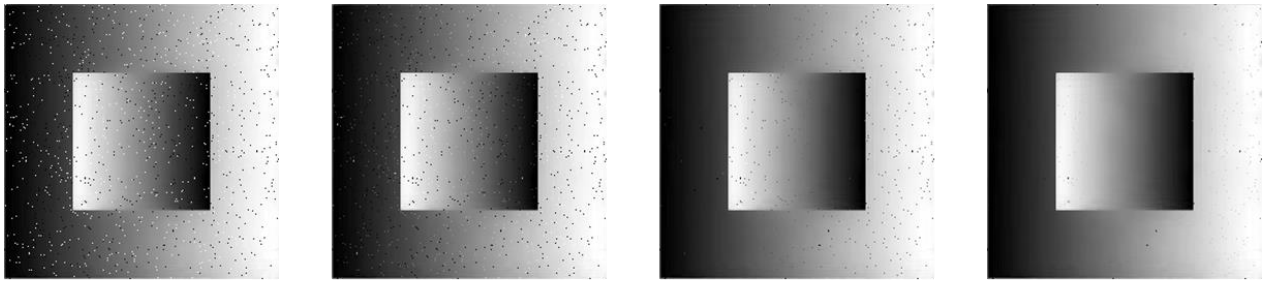

(a) Square with noisy $s = 0.02$ (b) Denoised image when $\alpha = 1$ (c) Denoised image when $\alpha = 1.5$ (d) Denoised image when $\alpha = 1.8$

Figure 4. Comparison of visual results for different values of α for the noisy image at $s = 0.02$.

In the third experiment, we added Gaussian noise at $\sigma = 20$ and salt-and-pepper noise at $s = 0.03$ to four images and explore the performance of the algorithm. We chose $\lambda = 0.009$, $\mu = 2.3$. Table 5 shows the values of PSNR, while Figure 5 shows the experimental results Figure 6 shows the original image, the noisy image, and the denoised image for different values of α (from 0.8 to 1.9). The third and fourth rows represent their corresponding contour map. The data from Table 5 indicate that a larger α yields better denoising performance. Consequently, the fractional-order TV model outperformed the traditional TV model under mixed noise.

Based on the PSNR values and denoised images from the first three experiments, we can see that the fractional-order TV model can effectively reduce the block effect and perform better than the TV model.

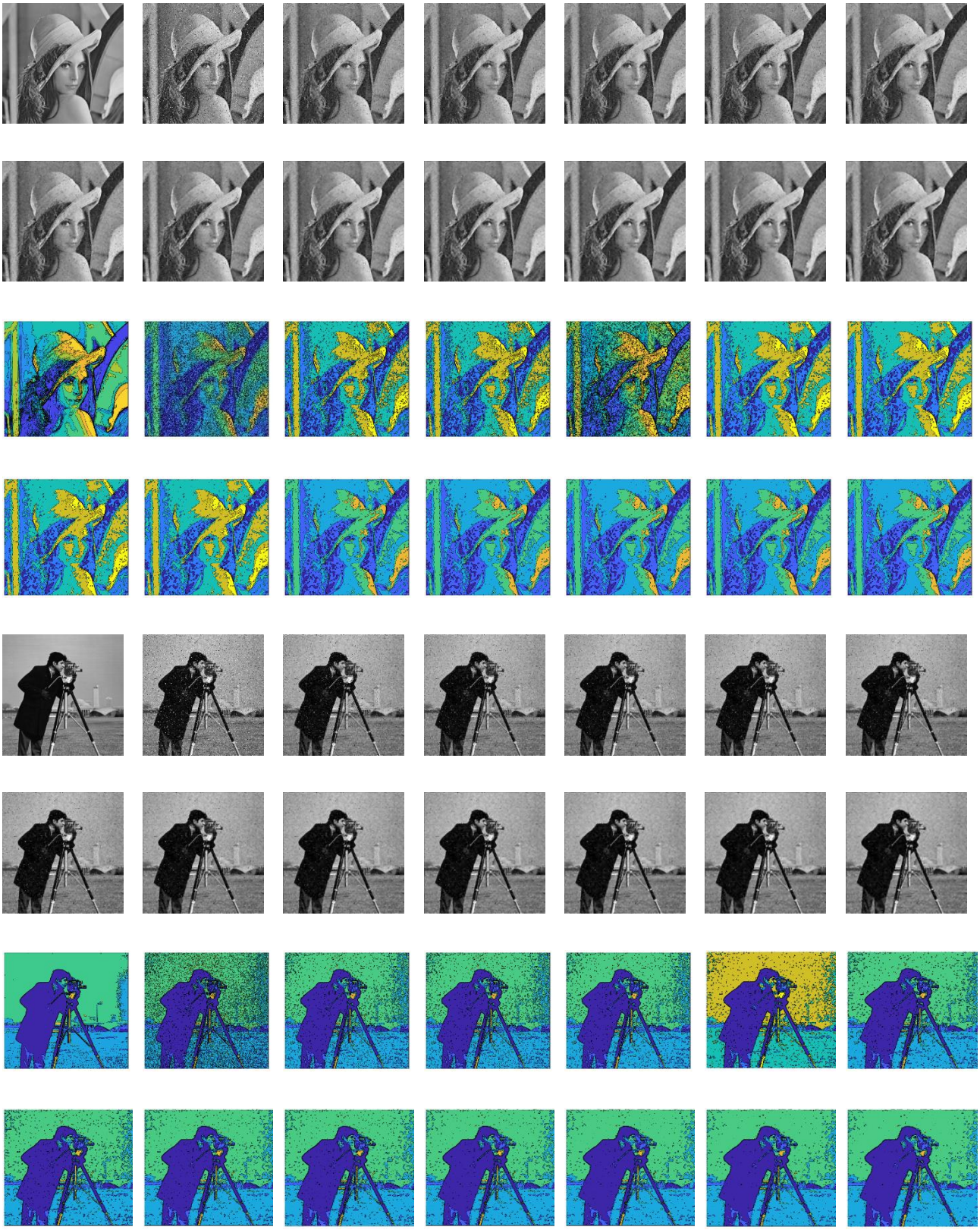

Figure 5. The original, noisy, and denoised images at different orders (from 0.8 to 1.9), where the third and fourth rows represent their corresponding contour map.

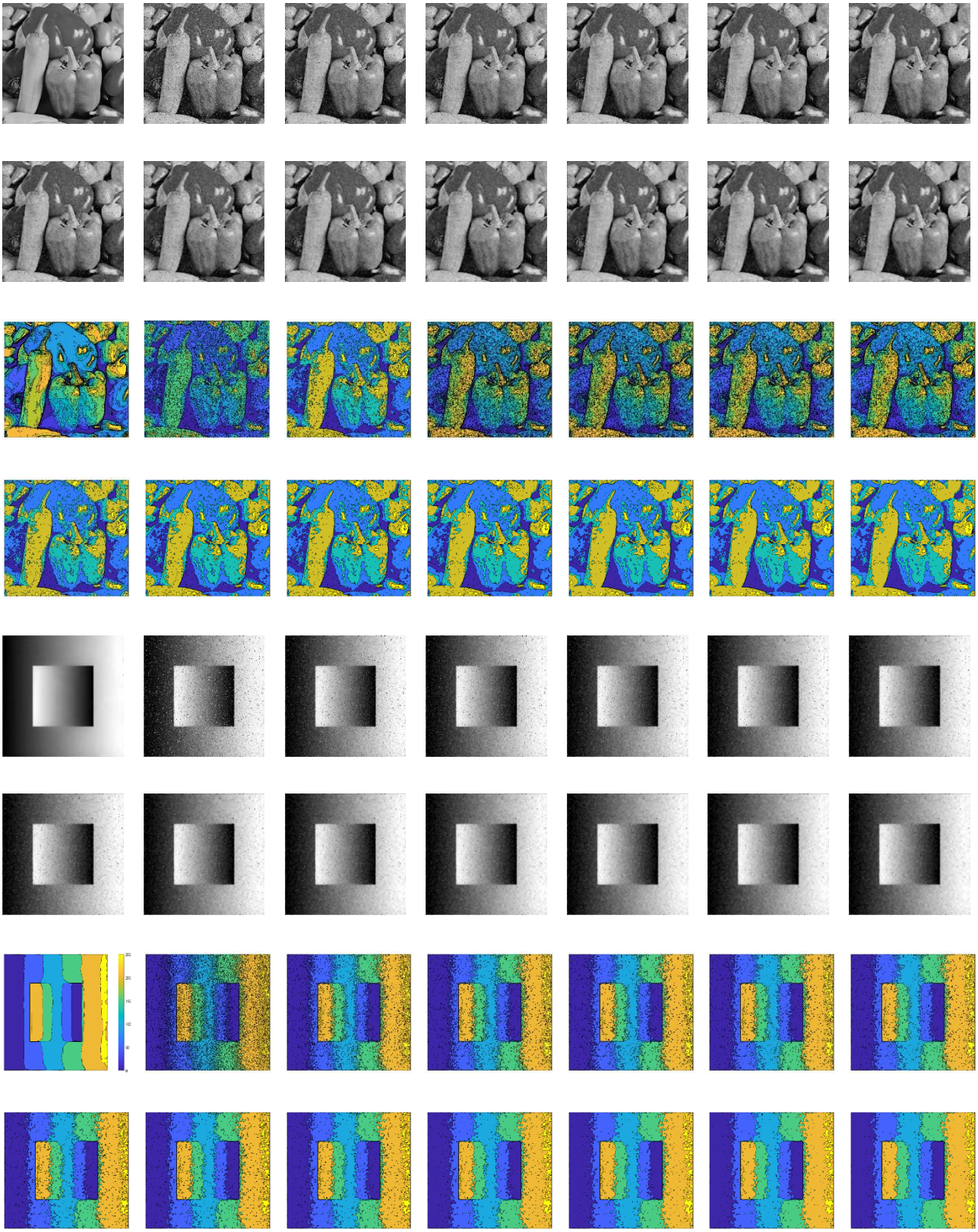

Figure 5. Continued.

Table 5. PSNR values for the noisy images with $\sigma = 20$ and $s = 0.03$.

α	Lena	Man	Pepper	Square
0.8	23.0276	22.7010	23.0907	22.5688
0.9	23.5519	23.128	23.5879	22.9819
1	24.0592	23.5512	24.0694	23.4123
1.1	24.6520	24.0576	24.6195	24.0678
1.2	25.3215	24.6112	25.2445	24.8745
1.3	25.8844	25.0583	25.7745	25.6832
1.4	26.3067	25.3817	26.1841	26.4623
1.5	26.6177	25.5930	26.4867	27.1617
1.6	26.8404	25.7059	26.7017	27.7913
1.7	27.0049	**25.7356**	26.8421	28.2917
1.8	27.1119	25.7179	**26.9169**	28.6416
1.9	**27.1679**	25.6679	26.9147	**28.8466**

The fourth experiment focused on the convergence of the algorithm. We applied $\alpha = 1.8$ as an example in the α range of 0.8 to 1.9. The PSNR value was recorded at each iteration. Figure 6 shows the experimental results. The blue line represents the noisy image results for $\sigma = 15, s = 0.01$, the red line represents the noisy image results for $\sigma = 20, s = 0.03$, and the yellow line represents the noisy image results for $\sigma = 20, s = 0.05$. From Figure 6, it is obvious that our proposed fractional-order TV denoising algorithm is convergent.

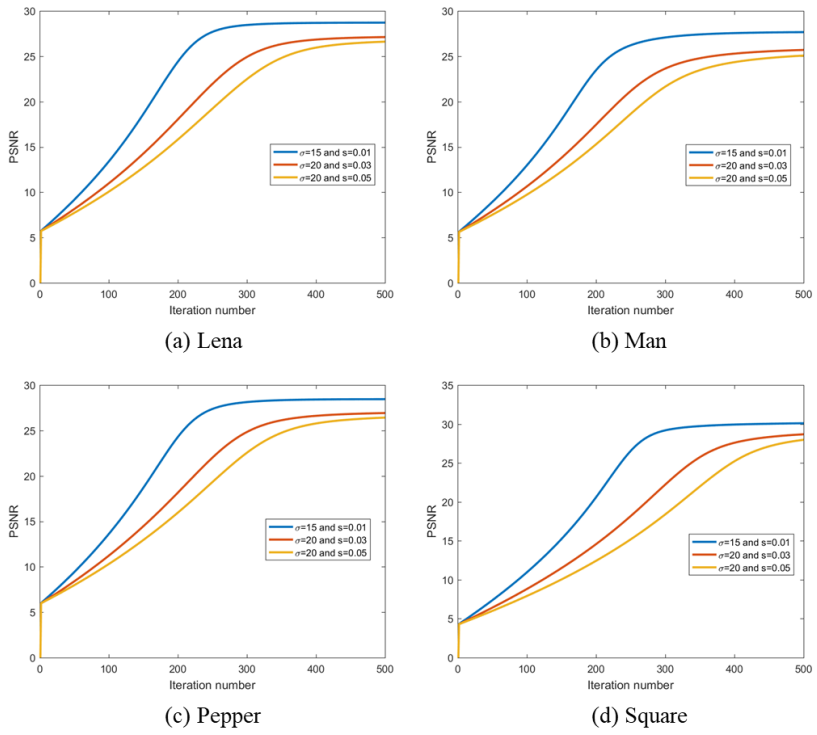

(a) Lena (b) Man

(c) Pepper (d) Square

Figure 6. Relationships between the iteration and PSNR.

Furthermore, we will show that our proposed model demonstrated good performance on the task of removing mixed noise. For this purpose, we added Gaussian noise at $\sigma = 20$ and salt-and-pepper noise at $s = 0.03$ to image 'Lena'. We chose $\alpha = 1.9$. Figure 7 shows the 60th and 100th rows of the 'Lena' image from a one-dimensional perspective. The original, noisy and denoised images are represented by black, pink and blue lines, respectively. The blue solid line and the black solid line nearly coincide, which indicates that our proposed model exhibited good denoising performance. Figure 8 shows that the histogram for the noisy image was completely different from that of the original image, while the histogram for the denoised image was similar to the histogram for the original image. We took a small part of the 'Lena' image and marked it with a red rectangle; the experimental results can be seen in Figure 9.

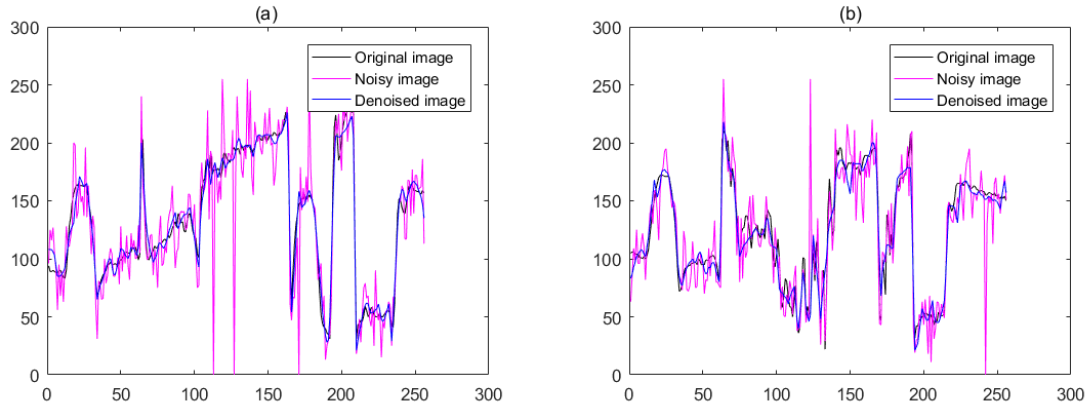

Figure 7. (a) The 60th line of the original, noisy, and restored images; (b) the 100th line of the original, noisy, and restored images.

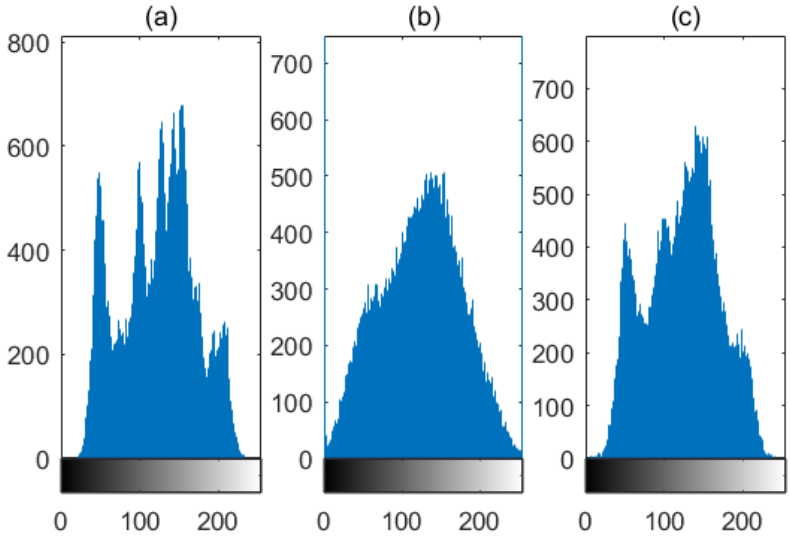

Figure 8. (a) Histogram of the original image; (b) histogram for the noisy image; (c) histogram for the denoised image.

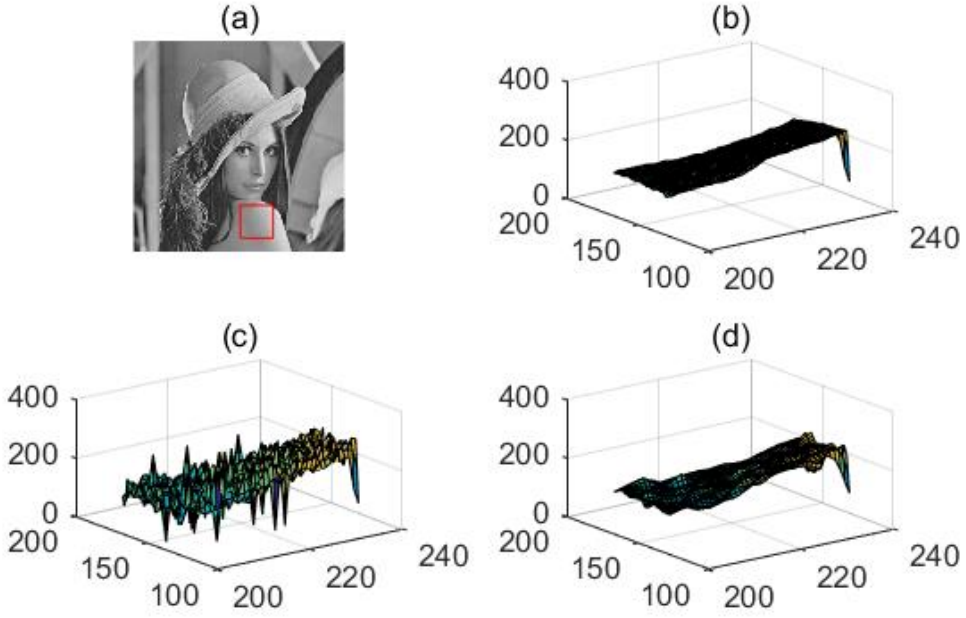

Figure 9. The three-dimensional surface map in results for (a) the red rectangular area of the 'Lena' image. (b) original image; (c) noisy image; (d) denoised image.

4. Conclusions

In this paper, we developed a fractional-order TV (L^1L^2/TV^α) model to remove mixtures of Gaussian noise and salt-and-pepper noise, by incorporating an L^1-data fidelity term and L^2-data fidelity term into the model. The existence of the solution of this model has been proved. We solved the proposed model by using the proximity algorithm, which prevents non-differentiability of the fractional order TV regularization terms. The convergence of the algorithm has been proved. The numerical experiments revealed the following: (1) The L^1L^2/TV^α model can effectively reduce the block effect and achieve better denoising performance than the L^1L^2/TV model. (2) The L^1L^2/TV^α model effectively removes the mixture of Gaussian noise and salt-and-pepper noise owing to the proximity algorithm. (3) In the L^1L^2/TV^α model, α should range from 0.8 to 1.9. Different images will have different optimal values of α.

Author contributions

Donghong Zhao: Conceptualization, funding acquisition, supervision, methodology; Ruiying Huang: Writing-original draft, writing-review & editing, software, formal analysis; Li Feng: Writing-original draft, software.

Use of AI tools declaration

The authors declare that they have not used artificial intelligence tools in the creation of this article.

Acknowledgments

This research was funded by Graduate Online Course Research Project of USTB (2024ZXB002), the National Natural Science Foundation of China (grant number 12371481) and Youth Teaching Talents Training Program of USTB (2016JXGGRC-002).

Conflict of interest

All authors declare no conflict of interest.

References

1. L. I. Rudin, S. Osher, E. Fatemi, Nonlinear total variation-based noise removal algorithms, *Physical. D*, **60** (1992), 259–268. https://doi.org/10.1016/0167-2789(92)90242-F
2. A. Chambolle, V. Caselles, D. Cremers, M. Novaga, T. Pock, An introduction to total variation for image analysis, *Radon Series Comp. Appl. Math.*, **9** (2010), 263–340. https://doi.org/10.1515/9783110226157.263
3. Y. L. You, M. Kaveh, Fourth-order partial differential equations for noise removal, *IEEE Trans. Image Process.*, **9** (2000), 1723–1730. https://doi.org/10.1109/83.869184
4. M. Lysaker, A. Lundervold, X. C. Tai, Noise removal using fourth-order partial differential equation with applications to medical magnetic resonance images in space and time, *IEEE Trans. Image Process.*, **12** (2003), 1579–1590. https://doi.org/10.1109/TIP.2003.819229
5. X. W. Liu, L. H. Huang, Z. Y. Gao, Adaptive fourth-order partial differential equation filter for image denoising, *Appl. Math. Lett.*, **24** (2011), 1282–1288. https://doi.org/10.1016/j.aml.2011.01.028
6. D. N. H. Thanh, V. B. S. Prasath, L. M. Hieu, A review on CT and X-Ray images denoising methods, *Informatica*, **43** (2019), 151–159. https://doi.org/10.31449/INF.V43I2.2179
7. D. N. H. Thanh, V. B. S. Prasath, L.T. Thanh, Total variation L^1 fidelity Salt-and-pepper denoising with adaptive regularization parameter, In: *2018 5th NAFOSTED Conference on information and computer science (NICS)*, 2018, 400–405. https://doi.org/10.1109/NICS.2018.8606870
8. T. F. Chan, S. Esedo, Aspects of total variation regularized L^1 function approximation, *SIAM. J. Appl. Math.*, **65** (2005), 1817–1837. https://doi.org/10.1137/040604297
9. W. Yin, D. Goldfard, S. Osher, The total variation regularized L^1 model for multiscale decomposition, *Multiscale Model. Simul.*, **6** (2007), 190–211. https://doi.org/10.1137/060663027
10. T. Chen, W. Yin, X. S. Zhou, D. Comaniciu, T. S. Huang, Total variation models for variable lighting face regularization, *IEEE Trans. Pattern Anal. Mach. Intell.*, **28** (2006), 1519–1524. https://doi.org/10.1109/TPAMI.2006.195
11. C. Zach, T. Pock, H. Bischof, A duality based approach for real time TV-L^1 optical flow, In: *Lecture notes in computer science*, Heidelberg: Springer, Berlin, **4713** (2007), 214–223. https://doi.org/10.1007/978-3-540-74936-3_22
12. K. Padmavathi, C.S. Asha, V. K. Maya, A novel medical image fusion by combining TV-L^1 decomposed textures based on adaptive weighting scheme, *Eng. Sci. Technol.*, **23** (2020), 225–239. https://doi.org/10.1016/j.jestch.2019.03.008

13. M. Hintermüller, A. Langer, Subspace correction methods for a class of nonsmooth and nonadditive convex variational problems with mixed L^1- L^2data-fidelity in image processing, *SIAM. J. Imaging Sci.*, **6** (2013), 34–73. https://doi.org/10.1137/120894130
14. Z. Gong, Z. Shen, K. C. Toh, Image restoration with mixed or unknown noises, *Multiscale Model. Simul.*, **12** (2014), 58–87. https://doi.org/10.1137/130904533
15. A. Langer, Automated parameter selection in the L^1-L^2-TV model for removing Gaussian plus impulse noise, *Inverse probl.*, **33** (2017), 074002. https://doi.org/10.1088/1361-6420/33/7/074002
16. D. N. H. Thanh, L. T. Thanh, N. N. Hien, S. Prasath, Adaptive total variation L^1 regularization for salt and pepper image denoising, *Optik*, **208** (2008), 163677. https://doi.org/10.1016/j.ijleo.2019.163677
17. R. W. Liu, L. Shi, S. C. H. Yu, D. Wang, Box-constrained second-order total generalized variation minimization with a combined $L^{1,2}$ data-fidelity term for image reconstruction, *J. Electron Imaging*, **34** (2015), 033026. https://doi.org/10.1117/1.JEI.24.3.033026
18. K. Bredies, K. Kunisch, T. Pock, Total generalized variation, *SIAM. J. Imaging Sci.*, **3** (2010), 492–526. https://doi.org/10.1137/090769521
19. D. Chen, Y. Chen, D. Xue, Fractional-order total variation image restoration based on primal-dual algorithm, *Abstr. Appl. Anal.*, **2013** (2013), 585310. https://doi.org/10.1155/2013/585310
20. D. Chen, H. Sheng, Y. Chen, D. Xue, Fractional-order variational optical flow model for motion estimation, *Philos. Trans. R. Soc. Lond. Ser. A Math. Phys. Eng. Sci.*, **371** (2013), 20120148. https://doi.org/10.1098/rsta.2012.0148
21. J. Zhang, Z. Wei, A class of fractional-order multi-scale variational models and alternating projection algorithm for image denoising, *Appl. Math. Model.*, **35** (2011), 2516–2528. https://doi.org/10.1016/j.apm.2010.11.049
22. J. Zhang, Z. Wei, L. Xiao, Adaptive fractional-order multi-scale method for image denoising, *J. Math. Imaging. Vis.*, **43** (2012), 39–49. https://doi.org/10.1007/s10851-011-0285-z
23. D. Chen, S. Sun, C. Zhang, Y. Chen, D. Xue, Fractional-order TV-L^2 model for image denoising, *Cent. Eur. J. Phys.*, **11** (2013), 1414–1422. https://doi.org/10.2478/s11534-013-0241-1
24. J. F. Cai, S. Osher, Z. W. Shen, Split Bregman methods and frame based image restoration, *Multiscale Model. Simul.*, **8** (2009), 337–369. https://doi.org/10.1137/090753504
25. Z. Qin, D. Goldfarb, S. Ma, An alternating direction method for total variation denoising, *Optim. Methods Softw.*, **30** (2011), 594–615. https://doi.org/10.1080/10556788.2014.955100
26. C. A. Micchelli, L. Shen, Y. Xu, Proximity algorithms for image models: denoising, *Inverse Probl.*, **27** (2011), 045009. https://doi.org/10.1088/0266-5611/27/4/045009
27. Q. Li, C. A. Micchelli, L. Shen, Y. Xu, A proximity algorithm accelerated by Gauss-Seidel iterations for L^1 /TV denoising models, *Inverse Probl.*, **28** (2012), 095003. https://doi.org/10.1088/0266-5611/28/9/095003
28. C. A. Micchelli, L. Shen, Y. Xu, X. Zeng, Proximity algorithms for the L^1/TV image denoising model, *Adv. Comput. Math.*, **38** (2013), 401–426. https://doi.org/10.1007/s10444-011-9243-y
29. D. Chen, Y. Chen, D. Xue, Fractional-order total variation image denoising based on proximity algorithm, *Appl. Math. Comput.*, **257** (2015), 537–545. https://doi.org/10.1016/j.amc.2015.01.012
30. Y. H. Hu, C. Li, X. Q. Yang, On convergence rates of linear proximal algorithms for convex composite optimization with applications, *SIAM J. Optim.*, **26** (2016), 1207–1235. https://doi.org/10.1137/140993090

31. J. J. Moreau, Fonctions convexes duales et points proximaux dans un espace hilbertien, *Comptes rendus hebdomadaires des séances de l'Académie des sciences*, **255** (1962), 2897–2899.
32. P. L. Combettes, V. R. Wajs, Signal recovery by proximal forward-backward splitting, *Multiscale Model. Simul.*, **4** (2005), 1168–1120. https://doi.org/10.1137/050626090
33. X. Y. Yu, D. H. Zhao, A weberized total variance regularization-based image multiplicative noise model, *Image Anal. Stereol.*, **42** (2023), 65–76. https://doi.org/10.5566/ias.2837
34. J. M. Shapiro, Embedded image coding using zerotrees of wavelet coefficients, *IEEE Trans. Signal Process.*, **41** (1993), 3445–3462. https://doi.org/10.1109/78.258085
35. L. Rudin, P. L. Lions, S. Osher, Multiplicative denoising and deblurring: Theory and algorithms, In: *Geometric level set methods in imaging, vision, and graphics*, New York: Springer, 2003, 103–119. https://doi.org/10.1007/0-387-21810-6_6

AIMS Press